





Retrieving aerosol backscatter coefficient using coherent Doppler wind lidar

TIANWEN WEI,¹ MENGYA WANG,^{1,5} PU JIANG,² KENAN WU,¹ ZHEN ZHANG,^{1,3} JINLONG YUAN,¹ HAIYUN XIA,^{1,2,6}  AND SIMONE LOLLI⁴ 

¹*School of Atmospheric Physics, Nanjing University of Information Science and Technology, Nanjing 210044, China*

²*School of Earth and Space Science, University of Science and Technology of China, Hefei 230026, China*

³*National Center of Carbon Metrology (Fujian), Nanping 353011, China*

⁴*CNR-IMAA, Contrada S. Loja snc, Tito Scalo (PZ), 85050, Italy*

⁵*wmengya123@nuist.edu.cn*

⁶*hsia@ustc.edu.cn*

Abstract: Coherent Doppler wind lidar (CDWL) has been widely used for wind detection, but retrieving aerosol optical properties remains challenging, due to its high sensitivity to turbulence and beam focusing. This study comprehensively evaluates the capabilities and limitations of pulsed CDWL in retrieving aerosol backscatter/extinction coefficient profiles, with a special focus on calibration and error analysis. A self-calibration method for the telescope focus function is proposed and validated through horizontal observations. Both forward and backward retrieval approaches are reviewed, with and without auxiliary co-located measurements. Key sources of uncertainty, including the carrier-to-noise ratio (CNR), heterodyne efficiency, lidar constant, and assumed lidar ratio, are analyzed. It's indicated that maintaining a controlled system environment is important for achieving a stable heterodyne efficiency profile. The lidar constant, calibrated using non-precipitating thick stratocumulus clouds, can achieve an uncertainty within 15% at 1550 nm, but the uncertainty increases with wavelength, as predicted by Mie theory. Under typical clear-sky conditions, an assumed lidar ratio with a 20% relative error introduces a relative error of less than 2% in the backscatter coefficient, whereas the extinction coefficient error is entirely dependent on the assumed lidar ratio. The influence of turbulence is further assessed using an equivalent experimental setup. With the deployment of thousands of CDWL systems worldwide, the ability to retrieve aerosol optical properties alongside simultaneous wind measurements is expected to significantly enrich datasets for aerosol transport studies, fog monitoring, and joint inversions with other instruments.

© 2025 Optica Publishing Group under the terms of the [Optica Open Access Publishing Agreement](#)

1. Introduction

Coherent Doppler wind lidars (CDWL) provide accurate radial Doppler velocity measurements at high temporal and spatial resolution, by using Doppler-shifted backscattering from atmospheric aerosols or hydrometers [1]. Due to its robust system design and affordable cost, CDWL has been commercially available and widely applied in many fields, including atmospheric dynamics [2,3], aviation safety [4,5], wind energy [6,7], pollution transport monitoring [8,9] and precipitation microphysics [10–13].

Aerosol optical properties were generally measured using the direct-detection lidars [14–20], such as Mie scattering lidar, Raman lidar, high-spectral-resolution lidar (HSRL), which typically operate at short wavelengths, like 355 nm, 532 nm, 1064 nm, to achieve higher single-photon energy. The heterodyne coherent detection adopted in CDWL is essentially a single-mode detection which is sensitive to the phase variation of the aerosol backscattering light. Consequently, longer wavelengths, such as 1.5 μm , 2.0 μm , 10.6 μm , is preferred to achieve higher coherence.

When combining Doppler wind lidar and aerosol lidars, accurate aerosol backscatter signals and wind profiles can be obtained simultaneously [17,21]. This strategy undoubtedly provides more accurate atmospheric measurements but also increases system size and cost, and makes it less conducive to airborne and spaceborne applications. Given that CDWL also utilizes aerosol backscattering, a question arises: can CDWL be used to detect aerosol optical properties and how accurately?

Researchers have tried to retrieve aerosol optical properties from coherent Doppler wind lidar measurements, following the approach used in traditional Mie lidars. However, there are some significant differences between them. Firstly, the calibration of aerosol lidars is usually performed using the Rayleigh molecular backscatter from the stratosphere or the high troposphere [22,23]. However, this method is not applicable to a CDWL operating at a near-infrared wavelengths of 1.5 μm or longer, mainly due to the low intensity of the molecular backscatter caused by the λ^{-4} wavelength dependence of the Rayleigh backscatter intensity, and the low sensitivity of the coherent detection to broad-spectral molecular signals [1]. Secondly, the heterodyne efficiency in CDWL, which inherently stands for the degree of field match between the single-mode local oscillation (LO) light and the atmospheric backscattering light, will modulate the received signal profile, especially in the near field [24]. It works similarly to the overlap function in the biaxial Mie lidar systems but follows different laws. Theoretical calculations may not always be appropriate due to ideal assumptions [25]. Therefore, an experimental determination of heterodyne efficiency is necessary. Chouza et al estimated the heterodyne efficiency function of airborne CDWL using the power received from the same altitude by changing the altitude of the aircraft [26]. Pentikäinen et al performed the estimation for Halo Photonics StreamLine by comparing the vertical aerosol backscattering profiles measured by Doppler wind lidar and co-located ceilometers working at 910 nm by assuming similar aerosol extinction and scattering properties between the two wavelengths [27]. However, these methods are not applicable to independently operated ground-based wind lidars. Thirdly, the difference in atmospheric attenuation between the two types of lidar makes the inversion of aerosol optical properties to exhibit inconsistencies in the accuracy of aerosol extinction coefficient and backscattering coefficient. As pointed out by Fernald, under low aerosol concentration and/or long wavelengths, the retrieval of aerosol backscattering coefficient is more accurate, as it is less sensitive to errors of the assumed so-called lidar ratio than the extinction profile [23].

Retrieval of aerosol optical parameters from a single-wavelength aerosol lidar, either Mie scattering lidar or Doppler wind lidar, is an ill-posed problem, which needs priori assumption of the extinction to backscattering ratio (i.e., the lidar ratio). The solution is well established and known as the Klett-Fernald method [22,23]. However, the lidar ratio has a very large variability (ranging from about 20-120 sr for aerosols) and strongly depends on the aerosol type and microphysical characteristics such as size distribution, particle shape, complex refractive index, etc. Furthermore, a calibration region is also required, which might have a great influence on the solution, especially for lidar systems operating at longer wavelengths, as it is hard to lose the dependence on initial values due to low attenuation. Therefore, additional information is usually applied to reduce uncertainties. This can be provided by collocated measurements of sun photometer [28], visibility sensor [29], advanced Raman lidar [30] or HSRL lidar systems. In addition, special observation setups can also be exploited, such as, horizontal measurements [31] or return signals from cloud having known optical properties [32]. As a result, the primary aerosol property that can be independently derived from a CDWL system is the aerosol backscattering coefficient after careful calibration to heterodyne efficiency, lidar constant, and atmospheric attenuation. Given the limited availability of co-located, high-cost lidar systems, self-calibration of backscattering of CDWL provides a practical solution for simultaneous wind and aerosol detection. This approach enables a comprehensive quantitative analysis of aerosol distribution,

transport, and interactions with clouds and precipitation, making it particularly valuable for the post-processing of long-term measurement datasets.

In the following section, we provide an overview of the coherent lidar equation, distinguishing it from Mie lidars (e.g., ceilometers) from a theoretical perspective. In Sect. 3, we propose a calibration method for the focus function using horizontal measurements and discuss which aerosol optical properties can be derived from the calibration or additional information. In Sect. 4, we systematically analyze the sources and contributions of uncertainties in retrieving aerosol optical properties without relying on auxiliary information from collocated instruments, including factors such as CNR, heterodyne efficiency, lidar constant, and assumed lidar ratio. Additionally, the influence of turbulence is assessed through an equivalent experimental approach.

2. Aerosol properties from CDWL

2.1. Coherent lidar equation

In coherent lidar systems, the detection of signal intensity and frequency is achieved through the heterodyne or homodyne mixing of the local oscillator light with the signal light [33]. The lidar equation is commonly expressed using the carrier-to-noise ratio (CNR), as discussed by various authors at different levels of generality [34,24], and is presented here using the following form

$$CNR(R) = \frac{\eta_o c E}{2 h \nu B} \frac{A}{R^2} \eta_h(R) \beta(R) \exp \left[- \int_0^R 2\sigma(r) dr \right] \quad (1)$$

where CNR is the wideband carrier-to-noise ratio, varying as a function of range R from the instrument, η_o is the optical efficiency, c is the speed of light, E is the beam energy, h is Planck's constant, ν is the optical frequency, B is the receiver bandwidth, and A is the effective receiver area, η_h is the heterodyne efficiency, β and σ are the atmospheric backscattering and extinction coefficients, respectively.

The extinction coefficient σ can be decomposed into contributions of aerosols σ_a and molecules σ_m (including scattering and absorption), while the backscatter coefficient β only includes the contribution from aerosols.

$$\sigma = \sigma_a + \sigma_m \quad (2)$$

$$\beta = \beta_a \quad (3)$$

This can be attributed to two main factors. First, the intensity of Rayleigh scattering at wavelengths of 1.5 μm or longer is significantly weaker compared to Mie scattering. Second, molecular scattering exhibits spectral broadening on the order of GHz, which is much broader than the spectral width of aerosol scattering. Furthermore, coherent detection inherently acts as a narrowband filter in the frequency domain, making it insensitive to the broadband, low-intensity signals from Rayleigh scattering.

2.2. Heterodyne efficiency

In coherent Doppler lidar equation, heterodyne efficiency is a key factor influencing the intensity of the return signal. It represents the field matching between the single-mode local oscillation (LO) light and the atmospheric backscattering light, primarily determined by the beam diameter and the focus distance of the transmitted laser beam. For a monostatic system with an untruncated circular Gaussian beam emitter and a matched-filter receiver, the theoretical heterodyne efficiency

can be expressed as [24]

$$\eta_h(R) = \left[2 + 2 \left(\frac{\pi \omega_T^2}{\lambda} \right)^2 \left(\frac{1}{R} - \frac{1}{R_f} \right)^2 + 2 \left(\frac{\omega_T}{\rho_0} \right)^2 \right]^{-1} \quad (4)$$

where λ is the laser wavelength, ω_T and R_f are the $1/e^2$ effective radiance radius of a Gaussian beam and the effective radius of the phase curvature at the emitting plane respectively, ρ_0 is the so-called transverse field coherence length determined by turbulent intensity and laser transmission path length R in the atmosphere. The so-called telescope focus function, also termed coherent responsivity, is also commonly referred to by researchers [24,27]

$$T_f(R) = \frac{A}{R^2} \eta_h(R) \quad (5)$$

Figure 1 show the simulation results of theory heterodyne efficiency and corresponding telescope function at different R_f with a fixed ω_T , where the turbulence term is ignored. The results show strongly dependance on the value of R_f . For positive values, heterodyne efficiency reaches the maximum at the focal range (location of the beam waist), which is a little smaller than the value of R_f . For infinite R_f , the beam is collimated, and the heterodyne efficiency increases with the distance. Negative values mean divergent beam and, the heterodyne efficiency is always smaller than that of collimated beam. In all cases, the heterodyne efficiency converges to the far-field limit.

$$\eta_h(R \gg R_f) = \left[2 + 2 \left(\frac{\pi \omega_T^2}{\lambda} \right)^2 \left(\frac{1}{R_f} \right)^2 \right]^{-1} \quad (6)$$

where the turbulence is ignored, and its influence will be examined and discussed in section 4.5. Obviously, the existence of atmospheric turbulence will reduce the efficiency of heterodyne, especially in the far field.

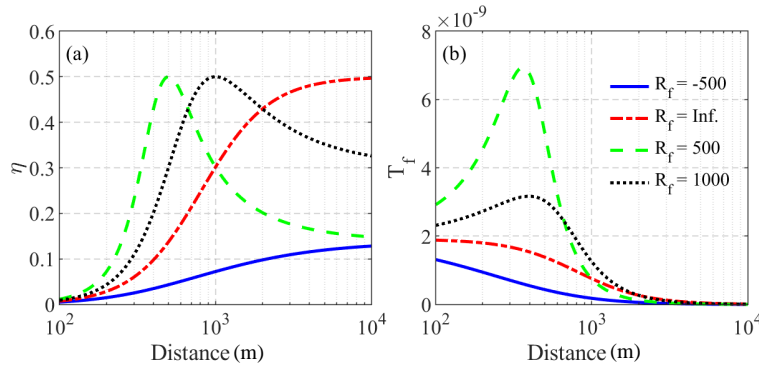


Fig. 1. Simulation of (a) heterodyne efficiency and corresponding (b) telescope focus function at different focal parameter R_f with $\omega_T = 2\text{cm}$.

According to the Van Cittert-Zernike Theorem [35], the receiver efficiency is inversely related to the area illuminated at the target plane, due to spatially incoherent scattering sources. Therefore, in continuous-wave Doppler lidar design, high gain is achieved by focusing the laser beam on the regions of interest. However, for pulsed coherent Doppler, the focus function modulates the received signal profile, leading to a misleading interpretation of the true aerosol distribution, particularly in the near field. This effect is analogous to the overlap function in the biaxial lidar systems, but with different far-field behaviors due to beam focusing and atmospheric turbulence.

Given that ground-based CDWL lidar systems are primarily used for detection and research on the atmospheric boundary layer near the surface, careful correction of the heterodyne efficiency is crucial for reliable retrieval of aerosol optical properties.

2.3. Aerosol backscatter coefficient

The profile of attenuated aerosol backscatter coefficient can be derived by rearrange the lidar equation

$$\beta'(R) = \frac{CNR(R) * R^2}{C_L \eta_h(R)} = \beta(R) \exp \left[- \int_0^R 2\sigma(r)dr \right] \quad (7)$$

where C_L is a lidar constant. Similar to ceilometers, the attenuated backscatter coefficient can be used in the same manner, such as determining cloud and boundary layer height [36,37], retrieving precipitation parameters [38–40]. Based on this, we further discuss the retrieval of backscatter coefficient $\beta(R)$ and extinction coefficient $\sigma(R)$ profiles.

As a problem inherent to all single-wavelength lidars, the solution of the lidar equation requires the assumption of a lidar ratio and a boundary value $\beta(R_0)$ or $\sigma(R_0)$ at a reference point R_0 , due to the unknown extinction-to backscatter relation and lidar constant, respectively. For coherent Doppler lidar systems, on the one hand, the molecule scattering is absent in the acquired signals, resulting in the Rayleigh calibration being impossible. On the other hand, due to long wavelengths, the atmospheric transmission term is close to unity and only gradually decreases with height. Therefore, any pronounced change in the lidar returns can be attributed to aerosol backscatter coefficient β and became the only aerosol property that can be derived quantitatively from coherent wind lidar measurement. Consequently, the extinction σ depends on the assumed lidar ratio S .

As pointed by Fernald, under conditions of low aerosol concentration and/or at long wavelengths, the retrieval of aerosol backscattering coefficient is generally more accurate, because it is less sensitive to errors of the assumed lidar ratio compared to the retrieval of the extinction profile [23,41]. This issue is further discussed in Section 3.2.

3. Method and retrieval

3.1. Focus function calibration

In this section, we calibrate the telescope focus function using horizontal measurements under the assumption of a homogenous aerosol distribution. As discussed in Sec.2.2, the heterodyne efficiency is influenced by the beam radius ω_T , the wavefront curvature radius R_f at the emitting plane, and the transverse field coherence length ρ_0 . Among these parameters, R_f has a substantial impact on the shape of the heterodyne efficiency curve and is highly sensitive to small variations in the focal length and position of the beam collimator. Therefore, its dependence on the temperature-induced deformation of the telescope [42] is also investigated by controlling and recording the inner temperature of the telescope. Although the beam radius ω_T is less sensitive to environment changes, theoretical calculation under ideal assumptions may introduce large errors. So, it is also determined from experiment combined with the R_f . The turbulence-related term ρ_0 is not considered after filtering out the measurements under high turbulence activities.

Assuming a homogeneous aerosol distribution, both the aerosol backscatter coefficient and extinction coefficient are constants. Therefore, the logarithmic form of attenuated aerosol backscatter coefficient $\ln\beta'(R)$ (or the telescope focus function corrected CNR) should exhibit a linear relationship with the range R .

$$\ln\beta'(R) = \ln\beta - 2\sigma R \quad (8)$$

To estimate the focus parameters, we perform linear fitting to the above profiles with guessed beam values of R_f and ω_T . Then calculate the mean square error of the fitting results, which can

be expressed as an optimization problem with the following objective function.

$$J(R_f) = \text{MSE}\{\ln\beta'(R; R_f, w) - \text{Linearfit}[\ln\beta'(R; R_f, w)]\} \quad (9)$$

Optimal beam parameters will generate perfect linear profile of $\ln\beta'(R)$. Therefore, the best estimation can be achieved when $J(R_f)$ reaches its global minimum. Figure 2(a) gives an example of the range corrected CNR and the linear fitting with the best estimation of the beam parameters. The result is obtained from horizontal measurement and averaged over 5 minutes to reduce random errors. The corresponding heterodyne efficiency is also given in the subplot.

Figure 2(b) shows the retrieved R_f at different system temperature T . Note that the results showing apparent inhomogeneous aerosol distribution and large fitting errors are filtered out from the analysis. The relationship between R_f and temperature T can be theoretically modeled as

$$R_f = \frac{1}{a + b * T} \quad (10)$$

where a and b are constants associated with the initial focus and material properties of telescope. Temperature fluctuations cause thermal expansion and contraction of the telescope, leading to significant changes in R_f and the corresponding focal range, thus affecting the echo signal curve, as shown in Fig. 3. This may cause artifacts and misleading interpretations of the CNR-based retrievals. For instance, variations in focal length due to uncontrolled system temperature can result in a significant discrepancy between the planetary boundary layer (PBL) height derived from CNR and that obtained from dynamic methods [43]. This underscores the importance of maintaining a stable and well-documented internal environment to ensure accurate focus information.

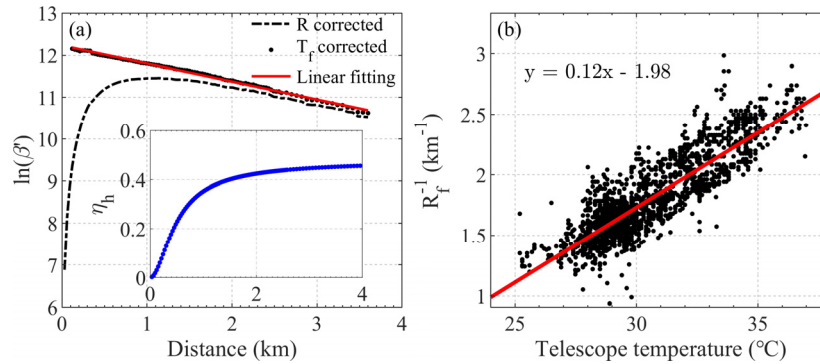


Fig. 2. (a) Example of retrieving heterodyne efficiency from horizontal measurements with range-corrected CNR (black dashed line), telescope focus function corrected CNR (black point) and linear fitting (read line). The corresponding heterodyne efficiency is also plotted in the subplot. (b) The scatter plot of the retrieved R_f with inner telescope temperature and corresponding fitting curve.

It is noteworthy that the experimentally retrieved beam radius ω_T at emitting plane is much smaller than the designed telescope radius. This discrepancy was also observed by Chouza in airborne CDWL, who attributed it to the limitations of certain underlying assumptions [26]. Pentikäinen retrieval using Halo Doppler lidars showed similar results [27]. Several factors may contribute to it, including an imperfect Gaussian beam profile (beam quality $M^2 > 1$), beam truncation at the telescope plane, beam aberrations and potential misalignment [44]. These observations emphasize the importance of determining beam parameters through experimental measurements rather than relying solely on theoretical calculations based on idealized assumptions.

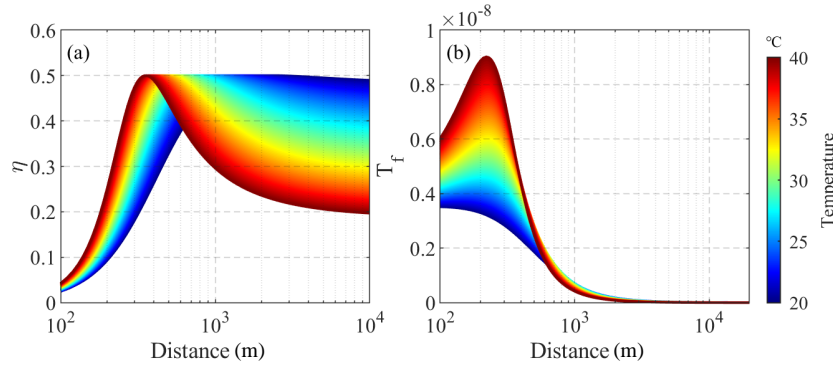


Fig. 3. (a) Heterodyne efficiency and (b) telescope focus function at various temperatures (indicated by colors). The temperature dependence is derived from the fitting results presented in Fig. 2(b).

An inaccurate value of ω_T in the model will lead to an incorrect inversion of R_f and thus wrong focus function correction. The uncertainty of the proposed focus function correction method is analyzed in Section 4.3.

3.2. Retrieval of backscatter coefficient

The forward and backward approaches are the two main methods used to retrieve aerosol optical properties in lidar systems [23]. The choice between these methods depends on the type of lidar, atmospheric conditions, and the availability of calibration data. For calibrated CDWL systems with a known lidar constant C_L and stable performance, the forward approach is typically preferred. It can be expressed as

$$\beta(R) = \frac{X(R)}{C_L - 2 \int_0^R S(r)X(r)dr} \quad (11)$$

with $X(R) = \frac{\text{CNR}(R) \cdot R^2}{\eta_h(R)} = C_L \beta'(R)$.

If a reference value $\beta(R_c)$ is given at a specific far field range R_c , the lidar constant C_L can be replaced and the backward integration can be expressed as

$$\beta(R) = \frac{X(R)}{\frac{X(R_c)}{\beta(R_c)} + 2 \int_R^{R_c} S(r)X(r)dr} \quad (12)$$

The backward approach, often based on Rayleigh calibration, is standard for UV and visible lidar systems, but is less effective for CDWLs at long wavelengths. This is due to the dominance of Mie scattering and the low sensitivity to molecular returns. In this section, we provide a concise review of the existing studies on the application of both forward and backward approaches for CDWLs, highlighting their respective limitations.

3.2.1. Forward approach

The basic principle of the forward approach is to calibrate the lidar constant C_L . This is equivalent to giving a reference value in the near end, as C_L can be determined using Eq. (7), if the aerosol properties β_a and σ_a are known. The advantage of the forward approach is that real-time reference value is not required, provided the system remains stable. For compact fiber-based CDWL systems, such stability is generally achievable. However, situations involving unknown

attenuation, such as rain or dust deposition on the telescope mirror surface, can compromise the method's accuracy and should therefore be avoided.

Most calibration techniques rely on return signals from targets with known optical properties, including ground-based hard targets [45], natural earth surface [46,47] and stratocumulus clouds [32]. However, ground calibration using hard targets suffers some challenges. For example, the calibration distance is limited due to the restrictions of target size and a well-characterized system heterodyne efficiency is necessary. Furthermore, in the low boundary layer, variable atmospheric transmission and turbulence further introduce uncertainties [45]. For airborne lidars, retroreflection signals from sea and ground surface are used for calibration. This approach offers advantages like reduced impact from path-integrated turbulence, but it demands strict experimental conditions and has high variability depending on the location. For instance, sea surface calibration is influenced by wind-driven waves and whitecaps, adding to uncertainty [48,49,26].

O'Connor proposed a calibration method for ceilometer using the backscatter from non-precipitating stratocumulus cloud that fully attenuate the transmitted laser. It was shown that the integrated attenuated backscatter coefficient is given by [32,50].

$$B = \int_{z_{base}}^{\infty} \beta'(r) dr = \frac{1}{2\eta S_{cloud}} T_{aerosol}^2 \quad (13)$$

where S_{cloud} is the lidar ratio of cloud, η is the multiple scattering factor, and $T_{aerosol}$ represents the lower atmospheric transmission from the ground to the cloud base height. When S_{cloud} and η are known and ignore $T_{aerosol}$, the lidar constant C_L can be determined by scaling the lidar signal until the integrated backscatter agrees with the theoretical value.

This method has been widely used for calibration of ceilometers [32,51] and has been extended to CDWL systems [52,53]. The lidar ratio S_{cloud} at $1.5 \mu\text{m}$ is suggested to be 20 sr [52]. Due to the very narrow field of view of CDWL (typically $50 \mu\text{rad}$ for pulsed systems), multiple scattering effects can be neglected (i.e. $\eta = 1$). Although this method requires stringent environmental conditions and can be time-consuming, it provides a simple self-calibration approach for long-term autonomous lidar operations. Figure 4 illustrates a typical time series of vertical profiles of lidar backscatter observed from the ground by the CDWL. The sharp decrease in backscatter at 2 km around 09:00-10:00 corresponds to melting layer [13]. After approximately 20:00, continuous thick stratocumulus clouds are observed at altitudes of 1 - 1.6 km. The apparent lidar ratio values were calculated from the integrated lidar backscatter using Eq. (13). The lidar ratio converging to 20 sr for different cloud heights and aerosol load further validates the accuracy of the focus function and aerosol attenuation correction below the cloud (see Sect. 4.3). Intermittent large values are mainly attributed to clear-sky or drizzle events, which should be excluded during calibration.

Auxiliary information from collocated instruments can also be used for calibration of CDWL. Chouza calibrated a $2 \mu\text{m}$ airborne CDWL by combining coincident measurements from ground-based Mie-Raman lidar (Portable Lidar Systems, POLIS) and AERONET sun photometers [26]. The sun photometer provided an extinction conversion factor between 532 nm (POLIS) and $2 \mu\text{m}$ (CDWL). By applying the least squares fit between the backscatter coefficient measured by the POLIS and the extinction-corrected signal measured by the CDWL, calibration constants for different aerosol types were derived and subsequently used for CDWL data during other flight periods. It should be noted that, both the backscatter and extinction coefficients were retrieved on the wavelength of 532 nm, as POLIS only provides the lidar ratio at this wavelength and a wavelength conversion factor of backscatter coefficient is included in the calibration constants. Dai calibrated the lidar constant C_L by comparing the integrated extinction profile from CDWL measurements with coincident aerosol optical depth (AOD) from a collocated sun-photometer [28]. In this method, the backscatter coefficient β recovered from the CDWL was converted

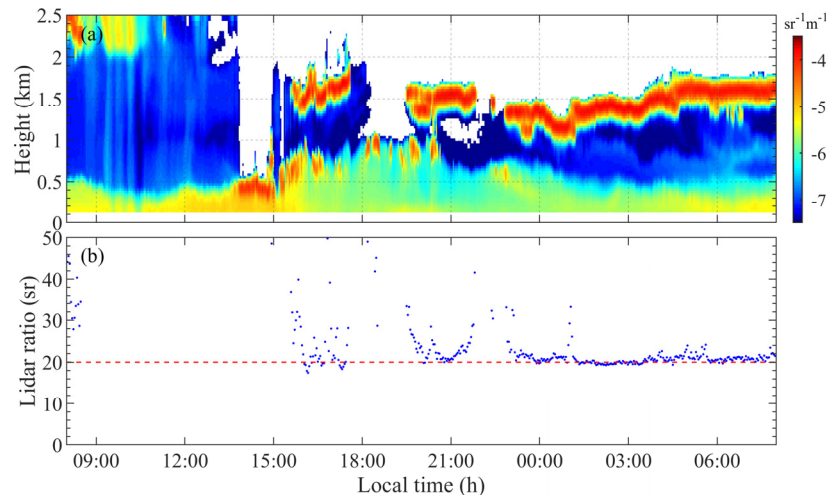


Fig. 4. Example of lidar constant calibration using thick non-precipitating liquid cloud. (a) Attenuated backscatter coefficient and (b) apparent lidar ratio observed on 11-12 February 2021, in Hefei, China. The sharp decrease in signal intensity at 2 km and 09:00-10:00 corresponds to the melting layer.

into an extinction profile using an assumed lidar ratio S . Thus, the calibrated lidar constant C_L will depend on the choice of lidar ratio. Besides, the retrieved C_L also shows large short-term variations, which is difficult to interpret as the lidar constant is expected to depend only on the system configuration and remain stable for a well-designed system. Zhang employed a visibility sensor for real-time near-ground reference measurements of the extinction coefficient to implement the forward integration Fernald method [29]. An empirical relationship [54] was used to convert visibility into extinction coefficient at $1.5 \mu\text{m}$. In this method, the retrieved extinction and backscatter coefficients depend on the measured visibility and assumed lidar ratio, respectively, while the lidar constant is excluded from the calculations.

3.2.2. Backward approach

The backward approach requires a reference value at the far end, which is typically determined using Rayleigh calibration. However, this method is unsuitable for CDWLs operating at a near-infrared wavelength (e.g., $1.5 \mu\text{m}$ or longer), primarily due to the low backscatter intensity governed by Rayleigh scattering law, and the low sensitivity of the coherent detection to broad-spectral molecular signals [1]. It is worth noting that recent studies have demonstrated the retrieval of Rayleigh scattering spectrum using specially designed coherent systems with wider detection bandwidth, shorter operation wavelength and longer integration time [55–57]. Although these results appear promising, further investigations are needed to improve SNR and validation. At present, retrieving the Rayleigh spectrum from commercial CDWLs remains infeasible, both in terms of hardware limitations and software capabilities.

An alternative method involves using coincident measurements from collocated Mie-Raman lidars, which provide independent inversion of aerosol extinction and backscatter coefficients. Li et.al. provided the reference value for a $1.5 \mu\text{m}$ CDWL by converting the aerosol extinction obtained at the Raman wavelength using the empirical Ångström exponent [30]. The backward integration was then applied to retrieve the aerosol extinction coefficient with an assumed lidar ratio $S = 50$. Zhang employed a collocated 532 nm Mie-scattering lidar to offer the reference value, applying a conversion factor k for the aerosol backscatter coefficient from 532 to 1550 nm. This factor was determined by scaling the retrieved β profile with the reference one at 532

nm using an iterative Fernald method until the two β profiles show the same trends. In their calculation, the lidar ratios for 532 nm and 1550 nm were assumed to be 50 and 30, respectively. Sensitivity tests indicated that the retrieved β exhibited almost linear dependence on the lidar ratios for both wavelengths [29].

Therefore, the backward approach is challenging for CDWLs due to the difficulty in providing stable and accurate far-field boundary values. As the insensitive dependence of backward integration on the initial value is generally not satisfied for the conditions of CDWL [23], unstable reference value may lead to time-varying artificial fluctuations in the retrieved profiles [30]. Proper selection of lidar ratio, based on aerosol types identification, is also important for accurate retrieval of aerosol extinction [58].

4. Uncertainty analysis

The uncertainty in the retrieved backscattering coefficient arises from random errors associated with the CNR, heterodyne efficiency, lidar constant, and assumed lidar ratio. In this section, we analyze the uncertainties contributed by each of these factors when retrieving the aerosol backscattering/extinction coefficients using the above calibration method without auxiliary information. Additionally, the influence of turbulence is also assessed through an equivalent experiment.

4.1. Uncertainty of CNR

In practices, the estimation of CNR ($\langle P_s \rangle / \langle P_n \rangle$) is performed on the spectral domain, after carefully noise correction [59]. It is equivalent to the estimation of backscattering signal power $\langle P_s \rangle$, assuming the noise power $\langle P_n \rangle$ to be known. The relative uncertainty of CNR can be calculated using an analytical expression and experimental CNR [60,61].

$$\varepsilon_{CNR} = \frac{\sigma_{CNR}}{CNR} = \frac{1}{\sqrt{M_p M_t}} \left(1 + \frac{1}{CNR} \right) \quad (14)$$

where M_p is the averaging pulse number, M_t is the number of coherence cells in a range gate which is determined by the pulse duration and range gate length. It is noted that the above equation gives the random error of the experimental CNR, while the systematic error related to data processing method can also significantly influence the results. Therefore, a very careful correction to the background noise is essential for unbiased estimation of CNR and further retrieval of aerosol optical properties [62,63].

4.2. Uncertainty of heterodyne efficiency

Based on the results of Sec. 3.1, the uncertainty in heterodyne efficiency is estimated through statistical analysis of the retrieved focus parameter R_f . Figure 5(a) shows the normalized probability distribution of residuals between the measured R_f^{-1} and the corresponding fitting results (see Fig. 2) under various telescope temperatures. The comparable variation magnitudes observed across different temperatures suggest that the random errors are independent of temperature. The aggregated statistical distribution of the residuals across all temperatures is shown in Fig. 5(b), along with the Gaussian fitting results.

Figure 6 illustrates two examples of the heterodyne efficiency curves under different conditions: one for a focused beam ($R_{f0} = 500\text{m}$) and another for a nearly collimated beam ($R_{f0} = 10\text{km}$), respectively. By varying R_f^{-1} within the range of standard deviation $\sigma_{R_f} = 0.164 \text{ km}^{-1}$ as given in Fig. 5(b), the variation in heterodyne efficiency is calculated, enabling the maximum relative error to be determined

$$\varepsilon_\eta = \max \left\{ \left| \frac{\Delta\eta(R_f)}{\eta(R_{f0})} \right| \right\} = \max \left\{ \left| \frac{\eta(R_f) - \eta(R_{f0})}{\eta(R_{f0})} \right| \right\} \quad (15)$$

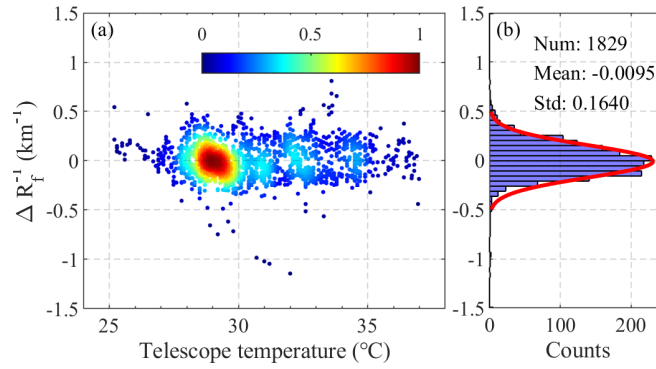


Fig. 5. (a) Residuals between the measured R_f^{-1} and the fitting results under different telescope temperatures. (b) Statistical distribution of the residuals over all temperatures and corresponding Gaussian fitting (red line).

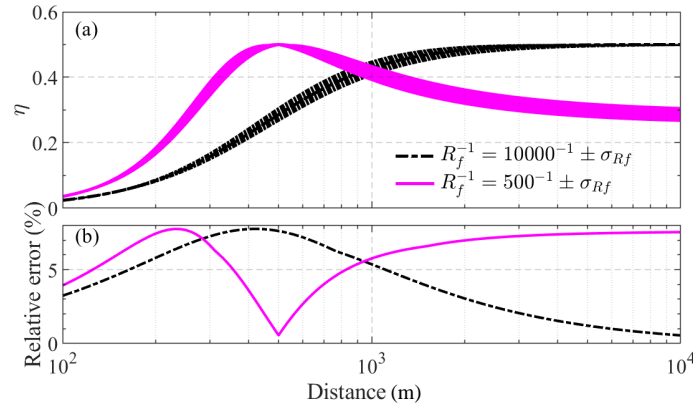


Fig. 6. (a) Simulation of heterodyne efficiency with R_f^{-1} centered at R_{f0}^{-1} (500 m and 10 km, respectively) and varying within the standard error σ_{Rf} . (b) Corresponding maximum relative error.

The relative error varies with range, reaching a maximum in the near field and a minimum at $R = R_{f0}$. For a focused beam, the relative error rapidly increases in the far field. In contrast, for a collimated beam, the error keeps decreasing between the near field maximum and far field R_{f0} . This indicates that, for typical detection range of 10 km, the heterodyne efficiency of a collimated beam is less sensitive to variations in the focus parameter R_f .

4.3. Uncertainty of lidar constant

As discussed in Section 3.1.1, the accuracy of the lidar constant C_L primarily depends on the microphysical properties of the stratocumulus clouds used for calibration, which are typically uncertain. According to Mie calculation results by Westbrook et al. (2010b), for liquid water droplets following a gamma distribution characterized by a median volume diameter D_0 (8–40 μm) and shape parameter μ (2–10), the lidar ratio S_{cloud} at 1.5 μm is $20 \text{ sr} \pm 20\%$.

Considering that most CDWLs operate at the fiber telecommunication wavelength of 1550 nm, we specifically calculated the lidar ratio S_{cloud} at this wavelength. As illustrated in Fig. 7(a), when D_0 lies within the range of 8 - 40 μm , S_{cloud} consistently falls within $20 \text{ sr} \pm 15\%$. Notably, as D_0 increases, S_{cloud} exhibits greater stability. Figure 6(b) presents the mean, maximum, minimum,

and standard deviation of S_{cloud} at various laser wavelengths, based on statistical analysis over the range of D_0 (8 - 20 μm) and μ (2 - 10), as suggested by [32,64]. The results reveal that the variability of S_{cloud} increases with wavelength, which can be attributed to the growing influence of Mie effects, primarily driven by contributions from smaller particles ($D_0 = 8 - 10 \mu\text{m}$). Therefore, for lidars operating at 2.0 μm , this calibration method may introduce greater uncertainties unless stricter constraints on cloud parameter are applied, such as excluding clouds with $D_0 < 10 \mu\text{m}$.

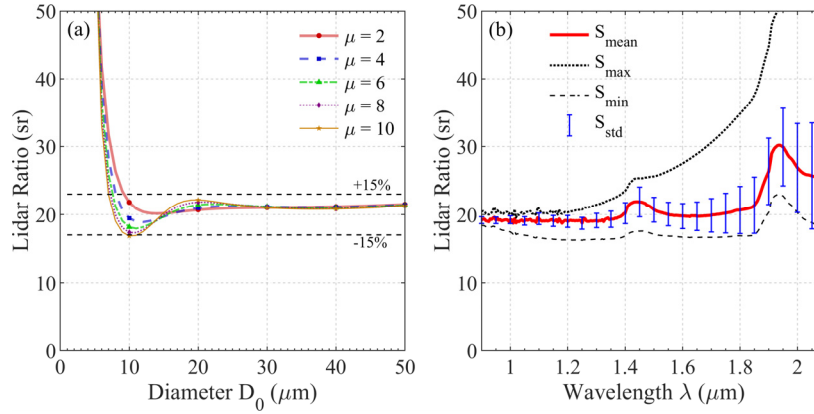


Fig. 7. (a) Theoretical lidar ratio S at 1550 nm as a function of median volume diameter D_0 for a gamma distribution of droplets with different values of shape parameters μ (2-10). Dashed black lines represents the boundary range of $20 \text{ sr} \pm 15\%$. (b) Theoretical lidar ratio S as a function of wavelength. The mean, maximum, minimum and standard deviation of S are calculated over the range of $D_0 = 8 - 20 \mu\text{m}$, and $\mu = 2 - 10$.

Additionally, as shown in Eq. (13), the transmission T_{aerosol}^2 within the boundary layer below the cloud base also affects the results. This factor is often neglected in previous studies due to its typically small values [65] or is addressed by filtering out results with high aerosol backscatter [32,51]. To quantify this influence, we performed simulations under typical turbid and clear atmospheric conditions, as illustrated in Fig. 8. The cloud base is set at two different heights of 0.5 km and 2 km, respectively, below which the aerosol optical depth τ_p and transmission T_{aerosol}^2 are summarized in Table 1.

Table 1. Aerosol optical depth τ_p at 1.5 μm , two-way transmission T_{aerosol}^2 of the atmosphere below cloud base (z_{base} , in kilometers) and its estimation value T_{est}^2 .

| | z_{base} | τ_p | T_{aerosol}^2 | T_{est}^2 | $T_{\text{est}}^2 / T_{\text{aerosol}}^2$ |
|--------|-------------------|----------|------------------------|--------------------|---|
| Clear | 0.500 | 0.013 | 0.974 | 0.979 | 1.005 |
| Turbid | 0.500 | 0.066 | 0.877 | 0.899 | 1.025 |
| Clear | 2.000 | 0.033 | 0.935 | 0.947 | 1.013 |
| Turbid | 2.000 | 0.167 | 0.716 | 0.759 | 1.060 |

For clear condition and clouds with $z_{\text{base}} < 0.5 \text{ km}$, the impact of T_{aerosol}^2 can be safely neglected, with an uncertainty of less than 3%. However, under turbid condition with a cloud base of 2 km, it reaches, reaching nearly 30%. This highlights the necessity of accounting for attenuation due to boundary layer aerosols under such conditions.

An iterative method can be employed to estimate T_{aerosol}^2 , utilizing the corrected C_L from the previous iteration and an assumed aerosol lidar ratio (set as 40 sr in the calculation of Table 1). As shown, even under turbid conditions with large z_{base} , the error in C_L can be reduced to less

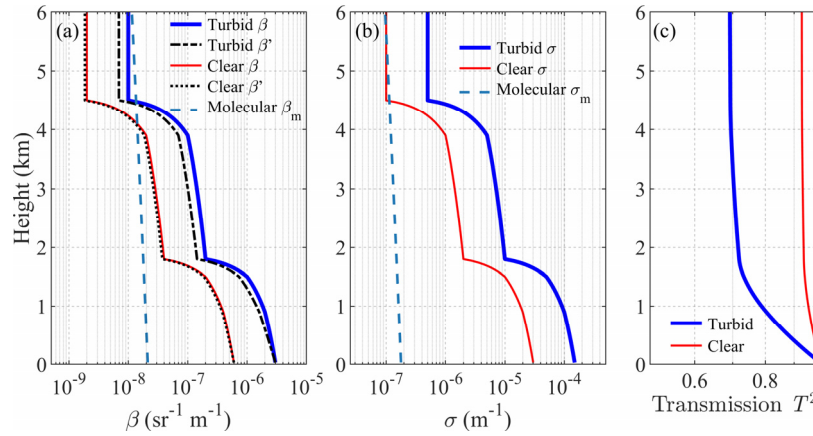


Fig. 8. Simulation model of (a) the aerosol backscatter coefficient profiles at $1.5 \mu\text{m}$ with different weather conditions (turbid/clear). The attenuated backscatter coefficient β' is also plotted in dashed black lines. (b) The aerosol extinction coefficient σ with assumed lidar ratio $S = 50$. The molecular extinction calculated from standard atmospheric model is plotted in black line. (c) Two-way atmospheric transmission.

than 6% when the estimated transmission is applied. Obviously, this estimation depends on the accuracy of the assumed lidar ratio, a factor discussed in detail in Sec.4.4.

It is worth noting that the strong backscattering signal from clouds can cause saturation problems in photon-counting detectors, such as those used in some ceilometers [41,50,65]. However, since CDWLs typically employ balanced PIN detectors with significantly larger linear dynamic ranges [66], saturation is not a concern in such systems.

4.4. Uncertainty of lidar ratio

The lidar ratio issue has been examined for aerosol lidar or ceilometer systems [67,68,41,50]. Here, we specifically revisit this parameter for typical values of aerosol optical properties at the wavelength of CDWL. Figure 9 shows the simulation results of the relative error in the retrieved aerosol backscatter and extinction coefficients using the aerosol model in Fig. 8.

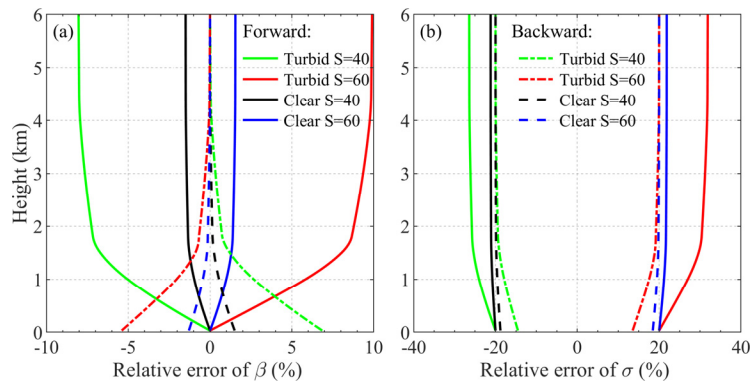


Fig. 9. Simulated relative error of retrieved (a) aerosol backscatter coefficient β and (b) aerosol extinction coefficient σ at different weather conditions (turbid/clear), different lidar ratios ($S = 40$ and 60) and different methods (forward/backward). The actual lidar ratio is set as $S = 50 \text{sr}$ in the simulation.

For both approaches, the error of attenuation correction using a wrong lidar ratio accumulates over the integration path length. Consequently, the relative error in β increases (decreases) with height for the forward (backward) approach. Nevertheless, the relative error of β is much smaller (less than 2%) at a typical clear atmospheric condition for both methods, suggesting that the systematic error of backscatter coefficient β is generally minor even with an incorrect assumption of lidar ratio S .

Although the backward method appears to yield more accurate results with smaller relative errors, it should be emphasized that the simulation results depend on the accurate prior information of $\beta(R_c)$ at the reference point, which is challenging to obtain in practice. Obtaining a low-relative-error reference value in the far field is much more difficult than in the near field due to the smaller absolute values involved.

Conversely, the relative error of σ is on the same order of magnitude as that of the lidar ratio itself, as shown in Fig. 9(b). For the backward method, this is primarily due to inaccuracies in the reference value, which is derived from an accurate β but an incorrect S . In fact, the extinction retrieval is independent on the lidar ratio S when a priori information of $\sigma(R_c)$ rather than $\beta(R_c)$ is given

$$\sigma(R) = \frac{X(R)}{\frac{X(R_c)}{\sigma(R_c)} + 2 \int_R^{R_c} X(r) dr} \quad (16)$$

As pointed out by Fernald, backward integration loses its dependence on the initial guess $\sigma(R_c)$ [23]. This is also evident in Fig. 9(b), which shows that a turbid atmosphere experiences less error in the near field. However, converging to the true σ requires a highly turbid atmosphere [69] or a long transmission path, which is a strict condition for CDWL due to its longer wavelength.

4.5. Uncertainty from turbulence

Up to now, the influence of refractive turbulence has been ignored. Its impact on heterodyne efficiency has been theoretically analyzed in previous studies [24,70,71]. The expression of transverse field coherence length ρ_0 is given by

$$\rho_0 = \left[2.91 k^2 \int_0^R C_n^2(r) (1 - r/R)^{5/3} dr \right]^{-3/5} \quad (17)$$

where $k = 2\pi/\lambda$ is the wavenumber, C_n^2 is the refractive index structure constant. Simulation results suggest that the impact of turbulence can be safely neglected for low values of C_n^2 up to $10^{-14} \text{ m}^{-2/3}$, and for most applications, it is also neglected when operating in the vertical direction [27].

We analysis the impact of refractive turbulence on the heterodyne efficiency using an experiment, based on the equivalent relation between the heterodyne efficiency and single-mode fiber coupling efficiency [72]. Detailed experimental information can be seen in previous work [73], where a single-mode fiber and multi-mode fiber are used as the two-channel receiver. As the fiber core of multi-mode fiber is much larger than that of the single-mode fiber, its coupling efficiency can be approximated as unity. Therefore, the ratio of the output signal intensity between the single-mode channel and multi-mode channel represents the single-mode fiber coupling efficiency and, consequently, heterodyne efficiency. The turbulence intensity (path-averaged C_n^2 here) is measured by the large aperture scintillometer (LAS). It is important to note that the biaxial telescope used in the experiment may exhibit a heterodyne efficiency curve different from that of a coaxial telescope, but this does not affect the analysis of turbulence effects.

Figure 10 shows three typical results measured under different turbulence intensities. Under weak turbulence conditions, the efficiency approaches 0.5 in the far filed. As turbulence increases, the efficiency decreases and becomes more pronounced with distance. The results suggests that the efficiency loss is approximately 10% in the far filed when the C_n^2 reaches $1.5 \times 10^{-14} \text{ m}^{-2/3}$.

Therefore, measurements under high turbulence intensities should be avoided when retrieving telescope focus function using horizontal measurements.

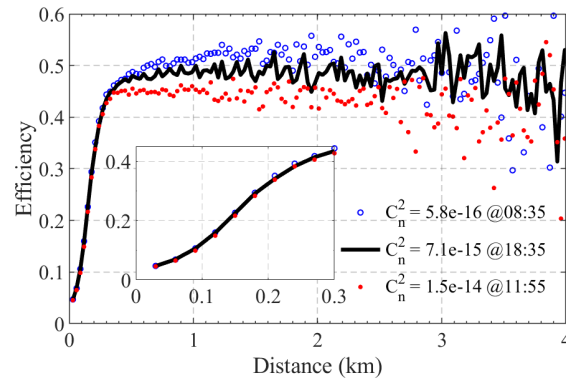


Fig. 10. Examples of the horizontally measured single-mode fiber coupling efficiency under three turbulence intensities at morning, noon, and afternoon, respectively. The zoomed-in view shows the details in the near-field within 300 m.

5. Discussion and conclusion

In this study, we comprehensively evaluated the capabilities and limitations of pulsed CDWL in retrieving aerosol backscatter/extinction coefficient profiles. A calibration method for the telescope focus function was validated using horizontal observations, assuming a homogeneous aerosol distribution. The results indicated that maintaining a controlled system environment is important for achieving a stable heterodyne efficiency profile. The calibration of lidar constant C_L using non-precipitating thick stratocumulus clouds was found can achieve an uncertainty within 15% at 1550 nm. However, the uncertainty increases with longer wavelength, suggesting that this calibration method may not be suitable for CDWL systems operating at wavelengths such as 2 μm . Additionally, aerosol attenuation within the boundary layer below the cloud was found cannot be ignored under most conditions. By applying an iterative method to estimate the aerosol transmission, the error in C_L was reduced to less than 6% even under turbid conditions with large cloud base heights, thus increasing the amount of data available for cloud-based calibration.

We reviewed forward and backward approaches for retrieving aerosol backscatter and extinction coefficient profiles, with and without auxiliary co-located measurements. It was concluded that the forward method is more suitable for CDWL, as the absence of molecular scattering precludes the use of traditional Rayleigh calibration. Under typical clear-sky conditions, an assumed lidar ratio with a 20% relative error introduces less than 2% relative error in the retrieved backscatter coefficient. However, the error of extinction coefficient was entirely dependent on the assumed lidar ratio, as was the case for aerosol optical depth (AOD). These conclusions were based on the assumption of a stable lidar constant, which is achievable with a typically compact all-fiber architecture. Any factors causing unexpected attenuation, such as rain or dust on the telescope lens, unmonitored changes in laser energy, would lead to failure of the method.

The influence of turbulence was also investigated using an experimental approach. The results suggested that the efficiency loss reaches approximately 10% in the far field when the C_n^2 is $1.5 \times 10^{-14} \text{ m}^{-2/3}$. However, for typically vertical measurements, the impact of turbulence will be reduced because of the weak turbulence activity above the mixing layer. Besides, the impact may also be mitigated by applying corrections based on turbulence information provided by the wind lidar itself.

With the rapid global deployment of thousands of pulsed CDWL systems, the retrieval of aerosol backscatter profiles has gained significant importance. This capability enables CDWL systems to function similarly to ceilometers, supporting aerosol layer and cloud detection [74]. By incorporating higher-order spectral moments, such as velocity, spectrum width, skewness, and depolarization information, CDWLs provide more accurate boundary layer classification and allow tracking transported aerosol pollutions [36,53]. Moreover, integrating backscatter profiles with ceilometer or cloud radar observations allows improved estimation of drizzle drop sizes and precipitation rates [38,75]. In future work, we will further assess the reliability and accuracy of the proposed calibration framework through long-term experiments and comparative analyses with other instruments under diverse atmospheric conditions.

Funding. National Natural Science Foundation of China (42405136).

Disclosures. The authors declare no conflicts of interest.

Data availability. Data underlying the results presented in this paper are not publicly available at this time but may be obtained from the authors upon reasonable request.

References

1. T. Fujii and T. Fukuchi, *Laser Remote Sensing* (CRC, 2005), Chap. 7.
2. E. J. O'Connor, A. J. Illingworth, I. M. Brooks, *et al.*, "A method for estimating the turbulent kinetic energy dissipation rate from a vertically pointing doppler lidar, and independent evaluation from balloon-borne in situ measurements," *J. Atmos. Oceanic Technol.* **27**(10), 1652–1664 (2010).
3. V. A. Banakh, I. N. Smalikho, and A. V. Falits, "Estimation of the height of the turbulent mixing layer from data of doppler lidar measurements using conical scanning by a probe beam," *Atmos. Meas. Tech.* **14**(2), 1511–1524 (2021).
4. P. W. Chan and A. M. Shao, "Depiction of complex airflow near hong kong international airport using a doppler LIDAR with a two-dimensional wind retrieval technique," *Meteorol. Z.* **16**(5), 491–504 (2007).
5. J. Yuan, L. Su, H. Xia, *et al.*, "Microburst, windshear, gust front, and vortex detection in mega airport using a single coherent doppler wind lidar," *Remote Sens* **14**(7), 1626 (2022).
6. Y. L. Pichugina, R. M. Banta, W. A. Brewer, *et al.*, "Doppler Lidar-Based Wind-Profile Measurement System for Offshore Wind-Energy and Other Marine Boundary Layer Applications," *J. Appl. Meteorol. Climatol.* **51**(2), 327–349 (2012).
7. N. Bodini, D. Zardi, and J. K. Lundquist, "Three-dimensional structure of wind turbine wakes as measured by scanning lidar," *Atmos. Meas. Tech.* **10**(8), 2881–2896 (2017).
8. D. Tang, T. Wei, J. Yuan, *et al.*, "Observation of bioaerosol transport using wideband integrated bioaerosol sensor and coherent doppler lidar," *Atmos. Meas. Tech.* **15**(9), 2819–2838 (2022).
9. M. Wang, T. Wei, S. Lolli, *et al.*, "A long-term doppler wind LiDAR study of heavy pollution episodes in western Yangtze River delta region, china," *Atmos. Res.* **310**, 107616 (2024).
10. M. Aoki, H. Iwai, K. Nakagawa, *et al.*, "Measurements of rainfall velocity and raindrop size distribution using coherent doppler lidar," *J. Atmos. Oceanic Technol.* **33**(9), 1949–1966 (2016).
11. T. Wei, H. Xia, J. Hu, *et al.*, "Simultaneous wind and rainfall detection by power spectrum analysis using a VAD scanning coherent doppler lidar," *Opt. Express* **27**(22), 31235–31245 (2019).
12. T. Wei, H. Xia, B. Yue, *et al.*, "Remote sensing of raindrop size distribution using the coherent doppler lidar," *Opt. Express* **29**(11), 17246–17257 (2021).
13. T. Wei, H. Xia, K. Wu, *et al.*, "Dark/bright band of a melting layer detected by coherent doppler lidar and micro rain radar," *Opt. Express* **30**(3), 3654–3663 (2022).
14. D. Müller, U. Wandinger, and A. Ansmann, "Microphysical particle parameters from extinction and backscatter lidar data by inversion with regularization: theory," *Appl. Opt.* **38**(12), 2346–2357 (1999).
15. S. Lolli, A. Delaval, C. Loth, *et al.*, "0.355-micrometer direct detection wind lidar under testing during a field campaign in consideration of ESA's ADM-Aeolus mission," *Atmos. Meas. Tech.* **6**(12), 3349–3358 (2013).
16. H. Xia, G. Shentu, M. Shangguan, *et al.*, "Long-range micro-pulse aerosol lidar at 1.5 μm with an upconversion single-photon detector," *Opt. Lett.* **40**(7), 1579–1582 (2015).
17. C. Wang, M. Jia, H. Xia, *et al.*, "Relationship analysis of PM_{2.5} and boundary layer height using an aerosol and turbulence detection lidar," *Atmos. Meas. Tech.* **12**(6), 3303–3315 (2019).
18. Z. Huang, Q. Dong, B. Chen, *et al.*, "Method for retrieving range-resolved aerosol microphysical properties from polarization lidar measurements," *Opt. Express* **31**(5), 7599–7616 (2023).
19. G.-J. van Zadelhoff, D. P. Donovan, and P. Wang, "Detection of aerosol and cloud features for the EarthCARE atmospheric lidar (ATLID): The ATLID FeatureMask (a-FM) product," *Atmos. Meas. Tech.* **16**(15), 3631–3651 (2023).
20. D. P. Donovan, G.-J. van Zadelhoff, and P. Wang, "The EarthCARE lidar cloud and aerosol profile processor (a-PRO): The a-AER, a-EBD, a-TC, and a-ICE products," *Atmos. Meas. Tech.* **17**(17), 5301–5340 (2024).

21. R. Engelmann, U. Wandinger, A. Ansmann, *et al.*, "Lidar observations of the vertical aerosol flux in the planetary boundary layer," *J. Atmos. Oceanic Technol.* **25**(8), 1296–1306 (2008).
22. J. D. Klett, "Stable analytical inversion solution for processing lidar returns," *Appl. Opt.* **20**(2), 211–220 (1981).
23. F. G. Fernald, "Analysis of atmospheric lidar observations: some comments," *Appl. Opt.* **23**(5), 652–653 (1984).
24. R. G. Frehlich and M. J. Kavaya, "Coherent laser radar performance for general atmospheric refractive turbulence," *Appl. Opt.* **30**(36), 5325–5352 (1991).
25. C. Hill, "Coherent focused lidars for doppler sensing of aerosols and wind," *Remote Sens.* **10**(3), 466 (2018).
26. F. Chouza, O. Reitebuch, S. Groß, *et al.*, "Retrieval of aerosol backscatter and extinction from airborne coherent doppler wind lidar measurements," *Atmos. Meas. Tech.* **8**(7), 2909–2926 (2015).
27. P. Pentikäinen, E. James O'Connor, A. Juhani Manninen, *et al.*, "Methodology for deriving the telescope focus function and its uncertainty for a heterodyne pulsed doppler lidar," *Atmos. Meas. Tech.* **13**(5), 2849–2863 (2020).
28. G. Dai, X. Wang, K. Sun, *et al.*, "Calibration and retrieval of aerosol optical properties measured with coherent doppler lidar," *J. Atmos. Oceanic Technol.* **38**(5), 1035–1045 (2021).
29. Y. Zhang, Y. Zheng, W. Tan, *et al.*, "Two practical methods to retrieve aerosol optical properties from coherent doppler lidar," *Remote Sens.* **14**(11), 2700 (2022).
30. M. Li, H. Xia, L. Su, *et al.*, "The detection of desert aerosol incorporating coherent doppler wind lidar and rayleigh-mie-raman lidar," *Remote Sens.* **15**(23), 5453 (2023).
31. S. Yang, J. Preißler, M. Wiegner, *et al.*, "Monitoring dust events using doppler lidar and ceilometer in Iceland," *Atmosphere* **11**(12), 1294 (2020).
32. E. J. O'Connor, A. J. Illingworth, and R. J. Hogan, "A technique for autocalibration of cloud lidar," *J. Atmos. Oceanic Technol.* **21**(5), 777–786 (2004).
33. P. Gatt and S. W. Henderson, "Laser radar detection statistics: a comparison of coherent and direct-detection receivers," in *Laser Radar Technology and Applications VI*, G. W. Kamerman and S. W. Henderson, eds. (2001), 4377, pp. 251–262.
34. C. M. Sonnenschein and F. A. Horrigan, "Signal-to-noise relationships for coaxial systems that heterodyne backscatter from the atmosphere," *Appl. Opt.* **10**(7), 1600–1604 (1971).
35. R. Mallart and M. Fink, "The van cittert-zernike theorem in pulse echo measurements," *J. Acoust. Soc. Am.* **90**(5), 2718–2727 (1991).
36. A. J. Manninen, T. Marke, M. Tuononen, *et al.*, "Atmospheric boundary layer classification with doppler lidar," *J. Geophys. Res.: Atmos.* **123**(15), 8172–8189 (2018).
37. S. Kotthaus, J. A. Bravo-Aranda, M. Collaud Coen, *et al.*, "Atmospheric boundary layer height from ground-based remote sensing: a review of capabilities and limitations," *Atmos. Meas. Tech.* **16**(2), 433–479 (2023).
38. C. D. Westbrook, R. J. Hogan, E. J. O'Connor, *et al.*, "Estimating drizzle drop size and precipitation rate using two-colour lidar measurements," *Atmos. Meas. Tech.* **3**(3), 671–681 (2010).
39. S. Lolli, M. Sicard, G. Vivone, *et al.*, "An automatic light rain detection algorithm on NASA MPLNET lidar observations in the frame of WMO GALION project," in *Remote Sensing of Clouds and the Atmosphere XXIV (SPIE*, 2019), 11152, pp. 40–46.
40. S. Lolli, L. P. D'Adderio, J. R. Campbell, *et al.*, "Vertically resolved precipitation intensity retrieved through a synergy between the ground-based NASA MPLNET lidar network measurements, surface disdrometer datasets and an analytical model solution," *Remote Sens.* **10**(7), 1102 (2018).
41. M. Wiegner, F. Madonna, I. Biniotoglou, *et al.*, "What is the benefit of ceilometers for aerosol remote sensing? An answer from EARLINET," *Atmos. Meas. Tech.* **7**(7), 1979–1997 (2014).
42. M. Hervé, Y. Poltera, and A. Haeferle, "An empirical method to correct for temperature-dependent variations in the overlap function of CHM15 k ceilometers," *Atmos. Meas. Tech.* **9**(7), 2947–2959 (2016).
43. L. Wang, W. Qiang, H. Xia, *et al.*, "Robust solution for boundary layer height detections with coherent doppler wind lidar," *Adv. Atmos. Sci.* **38**(11), 1920–1928 (2021).
44. Q. Hu, P. J. Rodrigo, T. F. Q. Iversen, *et al.*, "Investigation of spherical aberration effects on coherent lidar performance," *Opt. Express* **21**(22), 25670–25676 (2013).
45. R. T. Menzies and D. M. Tratt, "Airborne CO₂ coherent lidar for measurements of atmospheric aerosol and cloud backscatter," *Appl. Opt.* **33**(24), 5698–5711 (1994).
46. J. L. Bufton, F. E. Hoge, and R. N. Swift, "Airborne measurements of laser backscatter from the ocean surface," *Appl. Opt.* **22**(17), 2603–2618 (1983).
47. D. R. Cutten, J. Rothermel, M. A. Jarzembski, *et al.*, "Radiometric calibration of an airborne CO₂ pulsed Doppler lidar with a natural Earth surface," *Appl. Opt.* **41**(18), 3530–3537 (2002).
48. D. M. Tratt, R. T. Menzies, M. P. Chiao, *et al.*, "Airborne doppler lidar investigation of the wind-modulated sea-surface angular retroreflectance signature," *Appl. Opt.* **41**(33), 6941–6949 (2002).
49. Z. Li, C. Lemmerz, U. Paffrath, *et al.*, "Airborne doppler lidar investigation of sea surface reflectance at a 355-nm ultraviolet wavelength," *J. Atmos. Oceanic Technol.* **27**(4), 693–704 (2010).
50. D. Li, Y. Wu, B. Gross, *et al.*, "Capabilities of an automatic lidar ceilometer to retrieve aerosol characteristics within the planetary boundary layer," *Remote Sens.* **13**(18), 3626 (2021).
51. E. Hopkin, A. J. Illingworth, C. Charlton-Perez, *et al.*, "A robust automated technique for operational calibration of ceilometers using the integrated backscatter from totally attenuating liquid clouds," *Atmos. Meas. Tech.* **12**(7), 4131–4147 (2019).

52. C. D. Westbrook, A. J. Illingworth, E. J. O'Connor, *et al.*, "Doppler lidar measurements of oriented planar ice crystals falling from supercooled and glaciated layer clouds," *Q. J. R. Meteorol. Soc.* **136**(646), 260–276 (2010).
53. A. Hirsikko, E. J. O'Connor, M. Komppula, *et al.*, "Observing wind, aerosol particles, cloud and precipitation: Finland's new ground-based remote-sensing network," *Atmos. Meas. Tech.* **7**(5), 1351–1375 (2014).
54. R. Nebuloni, "Empirical relationships between extinction coefficient and visibility in fog," *Appl. Opt.* **44**(18), 3795–3804 (2005).
55. F. Chouza, B. Witschas, and O. Reitebuch, "Heterodyne high-spectral-resolution lidar," *Appl. Opt.* **56**(29), 8121–8134 (2017).
56. X. Chen, G. Dai, S. Wu, *et al.*, "Coherent high-spectral-resolution lidar for the measurement of the atmospheric Mie-Rayleigh-Brillouin backscatter spectrum," *Opt. Express* **30**(21), 38060–38076 (2022).
57. K. Kalmankoski and J. Toivonen, "Detection of molecular backscattering with a tapered fiber amplifier based coherent heterodyne lidar," *Opt. Express* **32**(11), 18831–18842 (2024).
58. Z. Huang, M. Li, J. Bi, *et al.*, "Small lidar ratio of dust aerosol observed by raman-polarization lidar near desert sources," *Opt. Express* **31**(10), 16909–16919 (2023).
59. S. Kameyama, T. Ando, K. Asaka, *et al.*, "Compact all-fiber pulsed coherent doppler lidar system for wind sensing," *Appl. Opt.* **46**(11), 1953–1962 (2007).
60. B. J. Rye and R. M. Hardesty, "Estimate optimization parameters for incoherent backscatter heterodyne lidar," *Appl. Opt.* **36**(36), 9425–9436 (1997).
61. F. Gibert, P. H. Flamant, J. Cuesta, *et al.*, "Vertical 2- μm heterodyne differential absorption lidar measurements of mean CO₂ mixing ratio in the troposphere," *J. Atmos. Oceanic Technol.* **25**(9), 1477–1497 (2008).
62. A. J. Manninen, E. J. O'Connor, V. Vakkari, *et al.*, "A generalised background correction algorithm for a halo doppler lidar and its application to data from Finland," *Atmos. Meas. Tech.* **9**(2), 817–827 (2016).
63. T. Wei, H. Xia, Y. Wu, *et al.*, "Inversion probability enhancement of all-fiber CDWL by noise modeling and robust fitting," *Opt. Express* **28**(20), 29662–29675 (2020).
64. N. L. Miles, J. Verlinde, and E. E. Clothiaux, "Cloud droplet size distributions in low-level stratiform clouds," *J. Atmos. Sci.* **57**(2), 295–311 (2000).
65. Y. Jin, N. Sugimoto, A. Shimizu, *et al.*, "Evaluation of ceilometer attenuated backscattering coefficients for aerosol profile measurement," *J. Appl. Rem. Sens.* **12**(04), 1 (2018).
66. S. Yu, K. Guo, S. Li, *et al.*, "Three-dimensional detection of CO₂ and wind using a 1.57 μm coherent differential absorption lidar," *Opt. Express* **32**(12), 21134–21148 (2024).
67. Y. Sasano and H. Nakane, "Significance of the extinction/backscatter ratio and the boundary value term in the solution for the two-component lidar equation," *Appl. Opt.* **23**(1), 11_1 (1984).
68. J. D. Klett, "Lidar inversion with variable backscatter/extinction ratios," *Appl. Opt.* **24**(11), 1638–1643 (1985).
69. H. G. Hughes, J. A. Ferguson, and D. H. Stephens, "Sensitivity of a lidar inversion algorithm to parameters relating atmospheric backscatter and extinction," *Appl. Opt.* **24**(11), 1609–1613 (1985).
70. R. Frehlich and L. Cornman, "Coherent Doppler lidar signal spectrum with wind turbulence," *Appl. Opt.* **38**(36), 7456–7466 (1999).
71. V. Banakh and I. Smalikho, *Coherent Doppler Wind Lidars in a Turbulent Atmosphere* (Artech House, 2013).
72. P. J. Winzer and W. R. Leeb, "Fiber coupling efficiency for random light and its applications to lidar," *Opt. Lett.* **23**(13), 986–988 (1998).
73. P. Jiang, H. Xia, J. Hu, *et al.*, "Estimation of atmospheric refractive index structure constant using an InGaAs/InP single-photon detector," *Opt. Lett.* **48**(23), 6104–6107 (2023).
74. R. J. Hogan, P. N. Francis, H. Flentje, *et al.*, "Characteristics of mixed-phase clouds. I: lidar, radar and aircraft observations from CLARE'98," *Q. J. R. Meteorol. Soc.* **129**(592), 2089–2116 (2003).
75. K. Tr  ummer, J. Handwerker, A. Wieser, *et al.*, "A synergy approach to estimate properties of raindrop size distributions using a doppler lidar and cloud radar," *J. Atmos. Oceanic Technol.* **27**(6), 1095–1100 (2010).